Available online at www.sciencedirect.com
ScienceDirect
International Journal of Heat and Mass Transfer 50 (2007) 4937–4947
International Journal of HEAT and MASS TRANSFER
www.elsevier.com/locate/ijhmt

Large eddy simulation of flow and heat transfer in a rotating ribbed channel

Joon Ahn [a], Haecheon Choi [b], Joon Sik Lee [b,*]

[a] Korea Institute of Energy Research, Daejeon, Republic of Korea
[b] School of Mechanical and Aerospace Engineering, Seoul National University, Republic of Korea

Received 1 May 2006; received in revised form 14 February 2007
Available online 12 July 2007

Abstract

The internal cooling passage of a gas turbine blade equipped with ribs is modeled as a rotating ribbed channel. The flow and heat transfer in the ribbed channel have been investigated by conducting large eddy simulations with a dynamic subgrid-scale model. The Reynolds number considered is 30,000 and rotation numbers are 0, 0.1 and 0.3. The time-averaged results show good agreement with the experimental data. By comparing the present data with those of the smooth channel, it is observed that the vortices shed from the rib induce strong wall-normal motions, and they are augmented on the trailing-wall side by the rotation, resulting in a significant increase in the heat transfer due to rotation. It is also shown that the similarity between the streamwise velocity and temperature is significantly destroyed by both the rotation and the rib itself.

Keywords: Ribbed channel; Large eddy simulation; Heat transfer; Rotation

1. Introduction

The cycle efficiency of a gas turbine can be enhanced through raising its inlet temperature. However, the inlet temperature can not go up beyond the material allowable temperature without appropriate blade cooling. Accordingly, various cooling techniques have been developed in the last several decades. For example, the internal cooling passage of blades is, in general, equipped with ribs to augment heat transfer by induced flow mixing and extended surface area [1].

The turbine blade with an internal cooling passage is commonly modeled as a rotating ribbed channel as shown in Fig. 1a. As is well known, flow and heat transfer characteristics inside the cooling passage depend on flow conditions and geometric configurations of the blade cooling system. Among geometric parameters, the ratios of the rib height to channel height ($=e/H$) and the rib pitch to height ($=p/e$) are most important (see Fig. 1b). From the hydrodynamic point of view, since the pressure drop is raised as the rib height increases, the optimum e/H is known to be around 0.1 [2,3]. The pitch also has an optimum, since it should be longer than the recirculation zone formed behind the rib. The recommended ratio of the rib pitch to height is about 10 for the Reynolds number range of interest [2,3].

Flow parameters such as the Reynolds number and rotation number are also of critical importance. The Reynolds number based on the bulk velocity, U_b, and hydraulic diameter, D_h, ranges from 10^4 to 10^5 in the internal cooling passage of the turbine blade. The Nusselt number increases with the Reynolds number for both smooth and ribbed channels [1,4]. However, the heat transfer enhancement rate by the rib, Nu/Nu_0, decreases as the Reynolds number increases, where Nu_0 is the Nusselt number on the smooth surface [3,4]. The rotation number, defined as $Ro = \Omega D_h/U_b$, ranges from 0.1 to 0.3 [1]. The rotation stabilizes the flow near the leading wall of the channel, while it destabilizes the flow along the trailing wall, and it also generates

* Corresponding author. Tel.: +82 2 880 7117; fax: +82 2 883 0179.
E-mail address: jslee123@snu.ac.kr (J.S. Lee).

0017-9310/$ - see front matter © 2007 Elsevier Ltd. All rights reserved.
doi:10.1016/j.ijheatmasstransfer.2007.03.049

Nomenclature

AR	aspect ratio of the channel ($=W/H$)
D_h	hydraulic diameter of the channel (m)
e	height of the rib (m)
f	friction factor
f_i	momentum forcing
h	heat transfer coefficient (W/m^2 K)
H	height of the channel (m)
k	thermal conductivity (W/m K)
m	mass source/sink
Nu	Nusselt number ($=hD_h/k$)
p	rib to rib pitch (m) or pressure (N/m^2)
Pr	Prandtl number ($=\nu/\alpha$)
q''	heat flux (W/m^2)
q_j	subgrid-scale heat flux, $q_j = \overline{Tu}_j - \overline{T}\overline{u}_j$
Q	second invariant of velocity gradient tensor
r	mean rotation radius (m)
Re	bulk Reynolds number ($=U_b D_h/\nu$)
Ro	rotation number ($=\Omega D_h/U_b$)
t	time (s)
T	temperature (K)
T_b	bulk temperature (K)
T_w	wall temperature (K)
U_b	bulk velocity (m/s)
u, v, w	streamwise, wall-normal and spanwise velocity components ($=u_1, u_2, u_3$)
u'	streamwise velocity fluctuation
u'^+	streamwise velocity fluctuation in wall unit
W	width of the channel (m)
x, y, z	Cartesian coordinates in the streamwise, wall-normal and spanwise directions ($=x_1, x_2, x_3$)

Greek symbols

α	thermal diffusivity (m^2/s)
ε_{ijk}	alternating epsilon
Φ	heat source/sink
ν	kinematic viscosity (m^2/s)
Θ	dimensionless temperature ($=(T - T_b)/(T_w - T_b)$)
Θ'	fluctuation of dimensionless temperature
Θ'^+	fluctuation of dimensionless temperature in wall unit
τ_{ij}	subgrid-scale stress, $\tau_{ij} = \overline{u_i u_j} - \overline{u}_i\overline{u}_j$
Ω	angular speed (rad/s)

Subscripts

rms	root-mean-square value
0	fully developed value in a smooth pipe

Superscript

$-$	time-averaged value or grid-filtered value

spanwise roll cells [5,6]. Thus, because of the rotation effect, heat transfer rate increases on the trailing wall but decreases on the leading wall [7,8].

The volume of experimental data that takes into account of the rotation effect is relatively small in the literature because of the measurement difficulty in a high speed rotating test rig equipped with sensors. In numerical simulations, the effect of anisotropy caused by the rotation can not properly be predicted using the standard k–ε turbulence model. Launder et al. [9] reported that the second moment closure is a minimum requirement for the simulation of the flow in the rotating system.

Even for the stationary case, the standard k–ε model does not accurately describe some important flow and thermal characteristics observed by experiments. For example, although predicting the mean flow field fairly well, the standard k–ε model fails to capture sharp peaks in the turbulence intensity variation observed near the rib. It also underpredicts the overall heat transfer rate, and does not simulate the high heat transfer rate in front of the rib. Acharya et al. [10] pointed out that the large-scale motion in the ribbed channel is not properly reflected in the k–ε model, and the wall function may cause the discrepancy in the heat transfer evaluation.

Recently, direct numerical simulation (DNS) and large eddy simulation (LES) have been attempted to overcome aforementioned problems. Ciafalo and Collins [11] conducted LES with the Smagorinsky model, and captured the high heat transfer region in front of the rib. Near the wall, however, their results overestimated the streamwise velocity, temperature drop and streak spacing due to the lack of resolution. Murata and Mochizuki [12] also per-

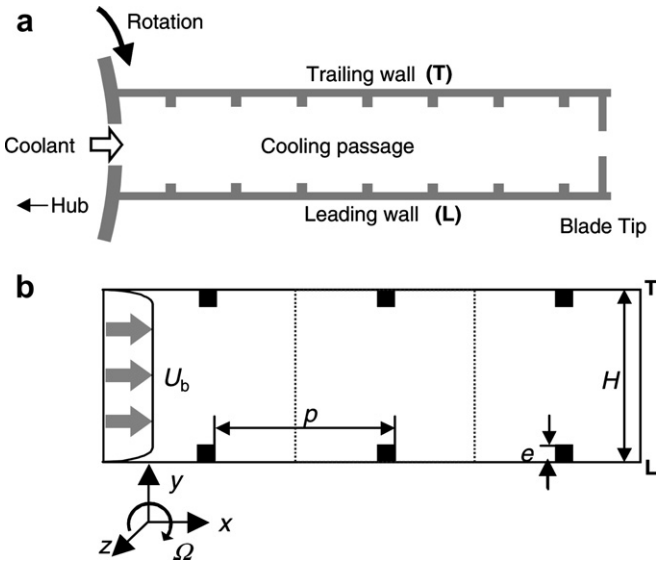

Fig. 1. Schematic of the cross section of a turbine blade with an internal cooling passage: (a) schematic diagram; (b) computational domain.

Table 1
Flow and geometric parameters

	Present	Murata and Mochizuki [12]	Cho et al. [25]	Liou and Hwang [26]	Kim et al. [27]
Method	LES	LES	Experiment	Experiment	Experiment
Re	30,000	4100	30,000	13,000	10,000
Ro	0, 0.1, 0.3	0–0.35	0	0	0–0.2
p/*e*	10	10	10	10	10
AR	∞	1, 2, 4	2	4	2
e/*H*	0.1	0.1	0.1	0.13	0.1

formed LES using the dynamic subgrid-scale model, but they fixed the subgrid-scale Prandtl number as 0.5. Moreover, their Reynolds number considered is roughly 10 times lower than that of a real gas turbine blade, which made it difficult to compare the results with the published experimental data. In the DNS of flow and heat transfer in a rib-roughened channel, the Reynolds numbers considered by Miyake et al. [13] and Nagano et al. [14] are even lower than that of Murata and Mochizuki [12]. Cui et al. [15] carried out LES at the Reynolds number comparable to that of a real engine cooling system, but they did not investigate heat transfer in their simulation. Most recently, Ahn et al. [16] and Tafti [17] performed LES including heat transfer in a ribbed channel at realistic Reynolds numbers, and showed excellent agreement with experimental data. However, all of the above works do not consider the rotation effect except Murata and Mochizuki's work [12].

In the present study, we conduct LES of flow and heat transfer in smooth and ribbed channels at the Reynolds number of 30,000. As for the ribbed channel, we fix the ratios of the rib pitch to height (=*p*/*e*) and the rib height to channel height (=*e*/*H*) as 10 and 0.1, respectively. Three Rotation numbers of $Ro = 0$, 0.1 and 0.3 are considered as listed in Table 1. Firstly, the time-averaged flow and thermal fields will be presented to discuss how the rotation affects the heat transfer on the leading and trailing walls, and secondly, the instantaneous data to examine the basic mechanism responsible for the change in the local heat transfer distribution by the rotation.

2. Numerical method

The governing equations for LES are the grid-filtered continuity, Navier–Stokes and energy equations for incompressible flow and heat transfer. The equation can be expressed as follows in the context of the immersed boundary method [18,19], including mass source/sink, m, momentum forcing, f_i, and the heat source/sink, Φ.

$$\frac{\partial \bar{u}_i}{\partial x_i} - m = 0, \tag{1}$$

$$\frac{\partial \bar{u}_i}{\partial t} + \frac{\partial}{\partial x_j}\bar{u}_i\bar{u}_j = -\frac{\partial p_{\text{eff}}}{\partial x_i} + \frac{1}{Re}\frac{\partial^2 \bar{u}_i}{\partial x_j \partial x_j} - \frac{\partial \tau_{ij}}{\partial x_j} + f_i - 2Ro\varepsilon_{ik3}\bar{u}_k, \tag{2}$$

$$\frac{\partial \overline{T}}{\partial t} + \frac{\partial}{\partial x_j}\overline{T}\bar{u}_j = \frac{1}{RePr}\frac{\partial^2 \overline{T}}{\partial x_j \partial x_j} - \frac{\partial q_j}{\partial x_j} + \Phi, \tag{3}$$

where the overbar represents a grid-filtered value, $\tau_{ij}(\equiv \overline{u_i u_j} - \bar{u}_i\bar{u}_j)$ is the subgrid-scale stress, and $q_j(\equiv \overline{Tu_j} - \overline{T}\bar{u}_j)$ is the subgrid-scale heat flux. Here, τ_{ij} and q_j are modeled employing the dynamic subgrid-scale model [20–22]. The rotation axis is z as shown in Fig. 1b. The system rotation induces the centrifugal force and the Coriolis force. The centrifugal force term is absorbed in the effective pressure given by

$$p_{\text{eff}} = \bar{p} - \frac{1}{2}Ro^2 r^2. \tag{4}$$

The last term in Eq. (2) represents the Coriolis force. The bottom wall corresponds to the leading wall, while the top wall is the trailing wall. The rotor blade cooling passage may have different channel orientation with respect to the rotating axis, but the rotation about the spanwise axis is reported to be much more influential to the heat transfer for both the smooth [7] and ribbed channels [23] than about other axes.

The numerical scheme to solve Eqs. (1)–(3) consists of a semi-implicit fractional step method and the second-order central difference scheme in space. The periodic boundary conditions are applied in the streamwise (x) and spanwise (z) directions. The no-slip and no-jump conditions are assumed on the channel wall and rib surface. These conditions on the rib surface can be satisfied by using an immersed boundary method. In this method, the momentum forcing, f_i, and heat source/sink, Φ, are provided in Eqs. (2) and (3) to satisfy the no-slip and no-jump conditions at the rib surface, respectively. The mass source/sink m in Eq. (1) is given to satisfy the continuity for the cell containing the immersed boundary. The numerical details are found in Kim et al. [18] and Kim and Choi [19].

The periodic boundary condition is justified using a sufficiently large computational domain. The streamwise domain size is set to be π times the channel height (=H) for the smooth channel, which has been tested for the turbulent channel flow by Kravchenko and Moin [24] at the Reynolds number comparable to the present study. As for the streamwise domain size of the ribbed channel, we conducted simulations with two different computational domain sizes, respectively, containing three pairs of ribs and one pair of ribs (see Fig. 1b for three pairs of ribs). They resulted in nearly the same time-averaged values in flow and heat transfer quantities. Therefore, we present results for a streamwise computational domain size containing only one pair of ribs. The spanwise domain size is

set to be 2.5π times the rib height, which is the same as one adopted by Kravchenko and Moin [24]. The two-point correlation at the separation distance of half the domain size shows zero fall-off for the ribbed channel.

The number of grid points is $48 \times 64 \times 48$ for the smooth channel, which is also the same as Kravchenko and Moin's [24]. It is $128 \times 128 \times 48$ for the ribbed channel. Grids are clustered near the wall and around the rib corner in the streamwise and wall-normal directions. Uniform grids are used in the spanwise direction. The grid sizes are; $\Delta x_{\min} \approx 0.0282e$, $\Delta x_{\max} \approx 0.2316e$, $\Delta y_{\min} \approx 0.0150e$, $\Delta y_{\max} \approx 0.2640e$, and $\Delta z = 0.1636e$. The simulations are carried out for 10,000 time steps to reach a fully developed flow. After the initial 10,000 time steps, additional 10,000 time steps ($tU_b/D_h = 5$) are integrated to obtain the statistics.

3. Results and discussion

3.1. Time-averaged quantities

When the distance between ribs is long enough (k-type roughness), four recirculation bubbles are known to exist; a recirculation bubble behind the rib, secondary one near the backward facing corner, a bubble on the top surface of the rib, and one in front of the forward facing corner [15–17]. Murata and Mochizuki [12] showed that the recirculation bubbles observed in the case of the non-rotating ribbed channel are merged into a big one which covers the leading wall when in rotation. However, the time-averaged streamlines obtained from the present study depicted in Fig. 2a show all the four characteristic recirculation bubbles both on the leading and trailing walls. We believe that the dissimilar flow structure is owing to the difference in the Reynolds number because other parameters considered in both studies are the same or within a comparable range (see Table 1). The Reynolds numbers in the present study and Murata and Mochizuki [12] are 30,000 and 4100, respectively. Although the four recirculation bubbles are observed on both of the walls, their size changes due to the rotation effect. Without rotation, the reattachment lengths on the leading and trailing walls are 4.37e. However, with rotation at $Ro = 0.3$, the length decreases to 3.98e on the trailing wall, but increases to 4.98e on the leading wall.

Comparing the streamlines with the isotherms shown in Fig. 2, the temperature contours are not so closely packed near the wall in the main recirculation zone, meaning that the heat transfer rates inside the recirculation bubble are lower than those at other locations where the contours are clustered near the wall. Another characteristics found in the temperature contour is the high curvature around the concave corner between the rib and the wall, indicating active heat transfer there. This phenomenon is found to be caused by the vortices around the corner [16]. The asymmetry caused by the rotation is also found in the thermal field.

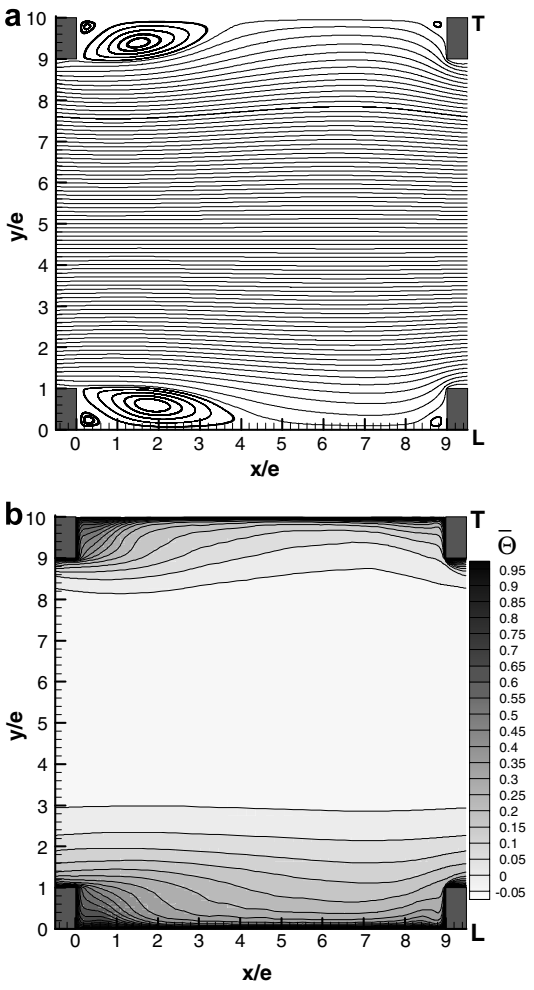

Fig. 2. Time-averaged flow and thermal fields inside the ribbed channel for $Ro = 0.3$: (a) streamlines; (b) isothermal lines.

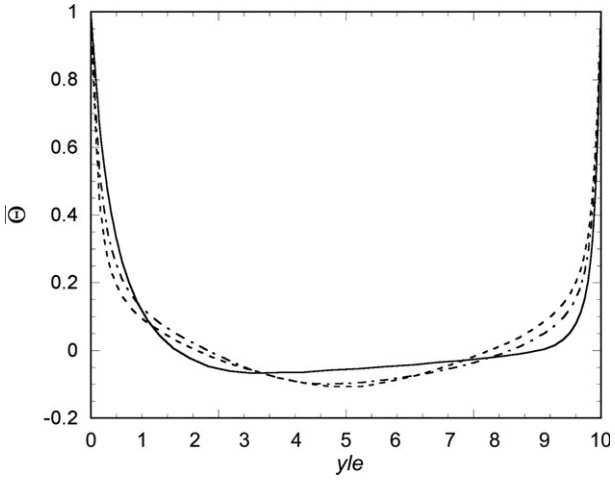

Fig. 3. Mean temperature profiles inside the smooth channel: ---, $Ro = 0$; -·-, $Ro = 0.1$; —, $Ro = 0.3$.

The cold area (bright gray) in the channel center is shifted toward the trailing wall.

Fig. 3 shows the variation of the time-averaged temperature profile due to rotation in the smooth channel. As the rotation number increases, the temperature gradient becomes relatively small on the leading wall ($y/e = 0$) while it becomes large on the trailing wall ($y/e = 10$). This indicates that the rotation suppresses heat transfer on the leading wall and augments it on the trailing wall. Another feature is that the temperature profile becomes flat in the channel core region as the rotation number increases. Similar trends are also observed in the rotating ribbed channel as can be seen in Fig. 4. However, in the rotating ribbed channel, the rotation effect on the temperature profile is relatively weak near the leading wall compared to that near the trailing wall. The temperature change in the channel core region due to the rotation is not so significant at $Ro = 0.1$ in the smooth channel (see Fig. 3), whereas considerable variation is observed in the ribbed channel.

The normalized Nusselt number for the non-rotating case is shown in Fig. 5, where Nu_0 is the Nusselt number on the smooth channel wall given by the Dittus–Boelter correlation as follows;

$$Nu_0 = 0.023 Re^{0.8} Pr^{0.4}. \quad (5)$$

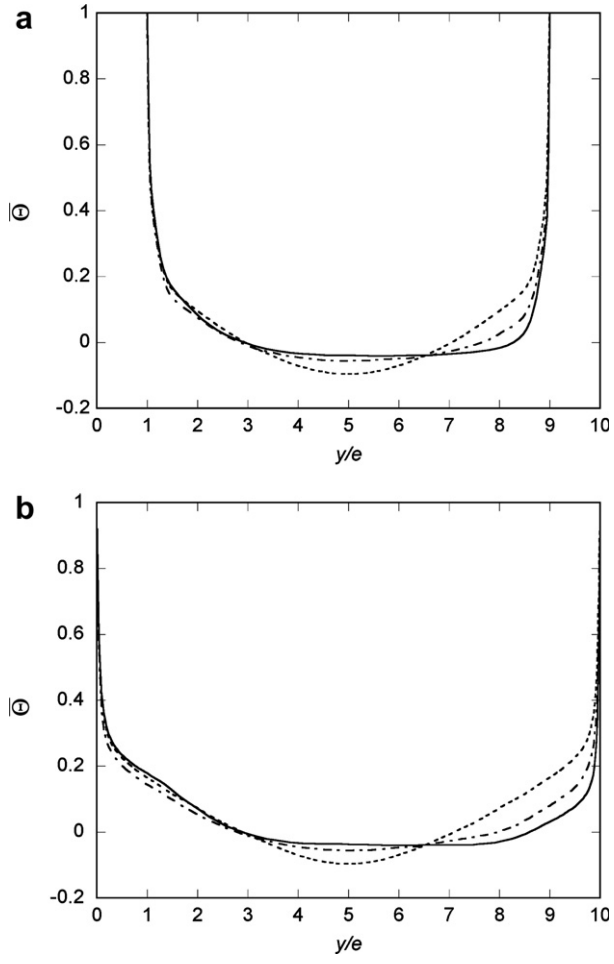

Fig. 4. Mean temperature profiles inside the ribbed channel: (a) $x/e = -0.5$; (b) $x/e = 4.5$. ---, $Ro = 0$; - · -, $Ro = 0.1$; —, $Ro = 0.3$.

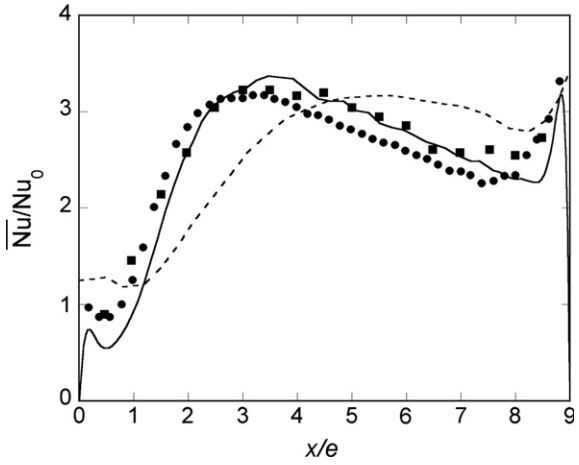

Fig. 5. Time-averaged Nusselt number between the ribs for $Ro = 0$: —, present; ●, Cho et al. [25]; ■, Liou and Hwang [26]; ---, Murata and Mochizuki [12].

As shown in Fig. 5, the Nusselt number from the present LES agrees well with the experimental data of Cho et al. [25] and Liou and Hwang [26]. The experiments and present LES commonly show a sharp peak in the Nusselt number distribution in front of the rib at about $x/e = 9$, and a broad peak around the reattachment point at about $x/e = 3$–4. The detail flow behavior responsible for this local Nusselt number distribution has been discussed by Ahn et al. [16]. The Nusselt number obtained by Murata and Mochizuki [12] also shows these peaks along the channel wall, but the broad peak locates further downstream compared with other results. This is because larger separation bubbles are formed at the lower Reynolds number considered in their study.

The Nusselt number distributions along the leading and trailing walls for the rotating cases are compared with the experimental data of Kim et al. [27] in Fig. 6. Although a strict comparison can not be made because the Reynolds number and aspect ratio of the channel are different (see Table 1), the present results are qualitatively in good agreement with experimental data. On the trailing wall (Fig. 6a), the Nusselt number increases with the rotation number. The local Nusselt number distribution from the present LES at $Ro = 0.1$ follows well that of Kim et al. [27]. Another thing to note is that the rotation effect on the heat transfer rate appears relatively stronger on the trailing wall than that on the leading wall as can be seen from both prediction and experiment. This trend coincides with the time-averaged temperature profiles as shown in Fig. 4. As the Rotation number increases, the heat transfer rate on the trailing wall is enhanced, while that decreases on the leading wall. On the leading wall, the quantitative agreement between the present and experimental data is not so good as on the trailing wall. This may be attributed to the fact that the effect of the Reynolds number is stronger on the leading wall than on the trailing wall, because the prediction and experiment agrees fairly well on the trailing wall

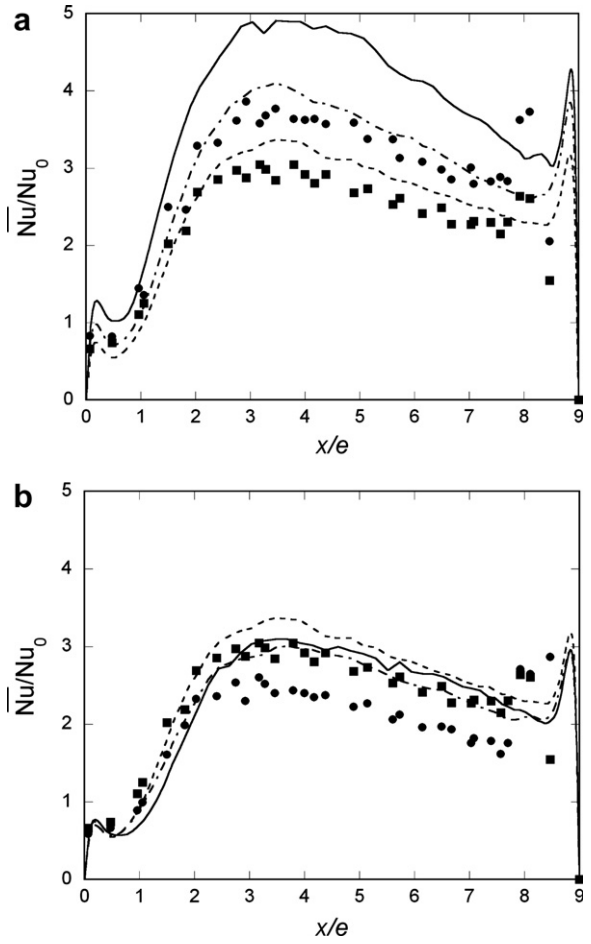

Fig. 6. Time-averaged Nusselt number between the ribs: (a) trailing wall; (b) leading wall. --- and ■, $Ro = 0$; - · - and ●, $Ro = 0.1$; —, $Ro = 0.3$. Here lines are from the present study and solid symbols are from Kim et al. [27].

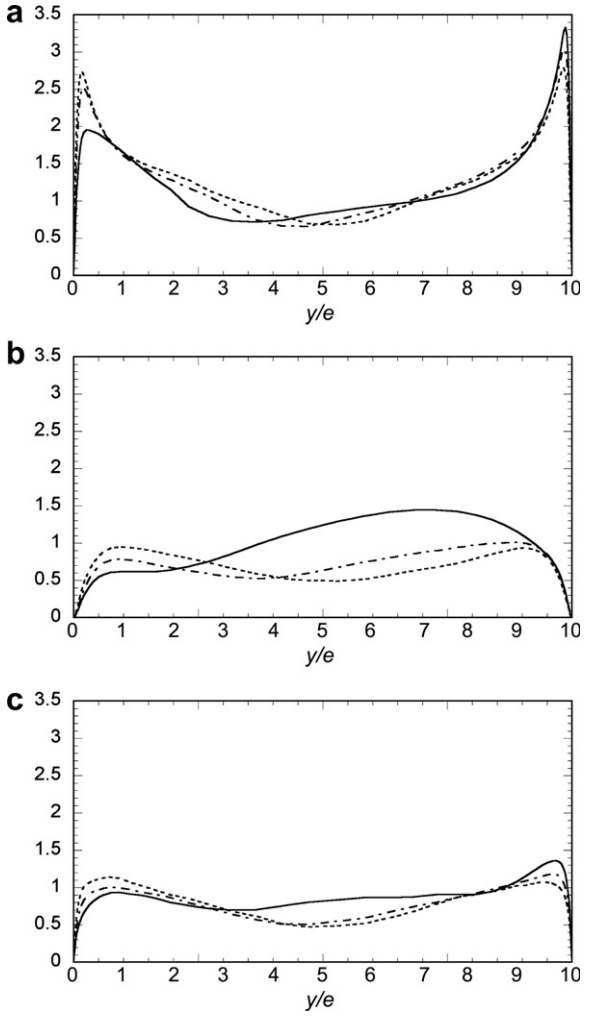

Fig. 7. Rms velocity fluctuations inside the smooth channel: (a) u_{rms}/u_τ; (b) v_{rms}/u_τ; (c) w_{rms}/u_τ. ---, $Ro = 0$; - · -, $Ro = 0.1$; —, $Ro = 0.3$.

even though the present Reynolds number is 30,000 which is three times as large as Kim et al.'s. The effect of the side wall may be another reason, which has not been considered in the present LES. The side wall produces the spanwise gradient of the streamwise velocity, which results in the secondary flow induced by the Coriolis force. The secondary flow is reported to suppress the turbulence intensity on the leading wall for the smooth channel [8]. This is consistent with the variations of the Nusselt number with Ro in the experiments and present LES as can be seen in Fig. 6b.

Fig. 7 shows turbulence intensity profiles in the rotating smooth channel. With rotation, turbulence intensities are amplified on the trailing side ($y/e = 10$) and suppressed on the leading side ($y/e = 0$). The turbulence intensity components of v_{rms} and w_{rms} significantly increase near the channel center at $Ro = 0.3$, but the increases in v_{rms} and w_{rms} are marginal at $Ro = 0.1$. However, direct numerical simulations by Kristoffersen and Andersson [6] showed a significant increase at $Ro = 0.1$ when $Re = 8000$. This implies that the rotation effect decreases with increasing Reynolds number.

Fig. 8 shows the contours of the rms velocity fluctuations in the non-rotating ribbed channel. The rms velocity fluctuations at the spanwise center of the channel agree well with Tafti's [17] LES data obtained for the channel aspect ratio ($=W/H$) of unity at $Re = 20{,}000$, indicating that the effect of the side wall is not prominent at the spanwise center even for such a small aspect ratio. All rms velocity fluctuations show their minimum behind the rib. The u_{rms} is highest at the rib top and also high along the separating shear layer. On the other hand, the v_{rms} is highest above the forward-facing wall of the rib. The maximum of w_{rms} is found near the forward-facing wall of the rib. The occurrence of maximum w_{rms} is related to the impingement of eddies on the forward-facing wall of the rib, which was already pointed out as a reason why the local peak of heat transfer occurs in front of the rib [16]. Near the reattachment point, w_{rms} is the largest among the three components, implying the existence of a strong spanwise motion there.

When the Coriolis force is imposed, the distribution of rms velocity fluctuations inside the ribbed channel becomes

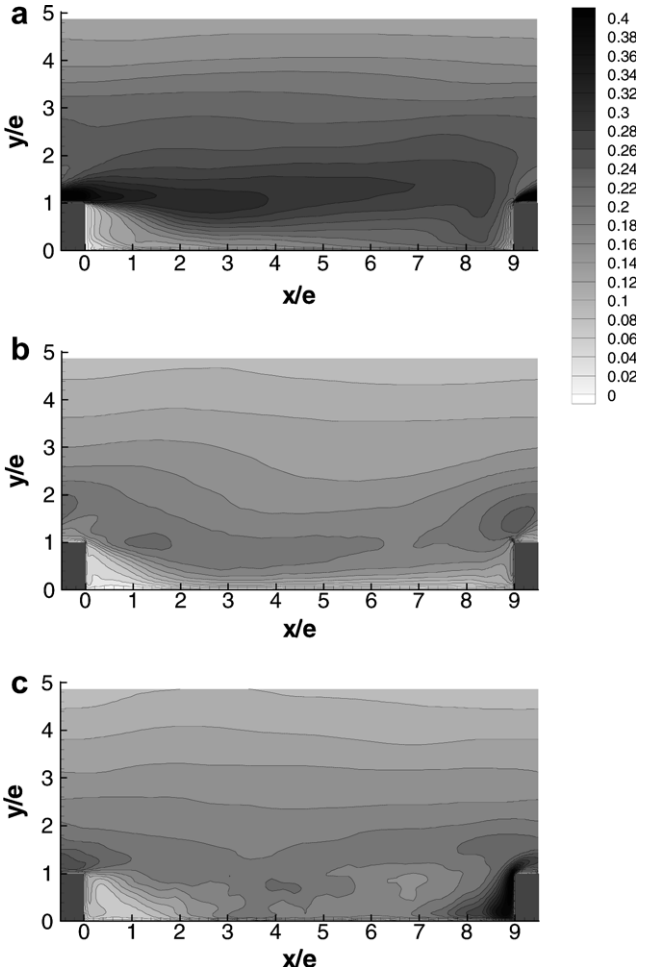

Fig. 8. Contours of the rms velocity fluctuations inside the ribbed channel for $Ro = 0$: (a) u_{rms}; (b) v_{rms}; (c) w_{rms}.

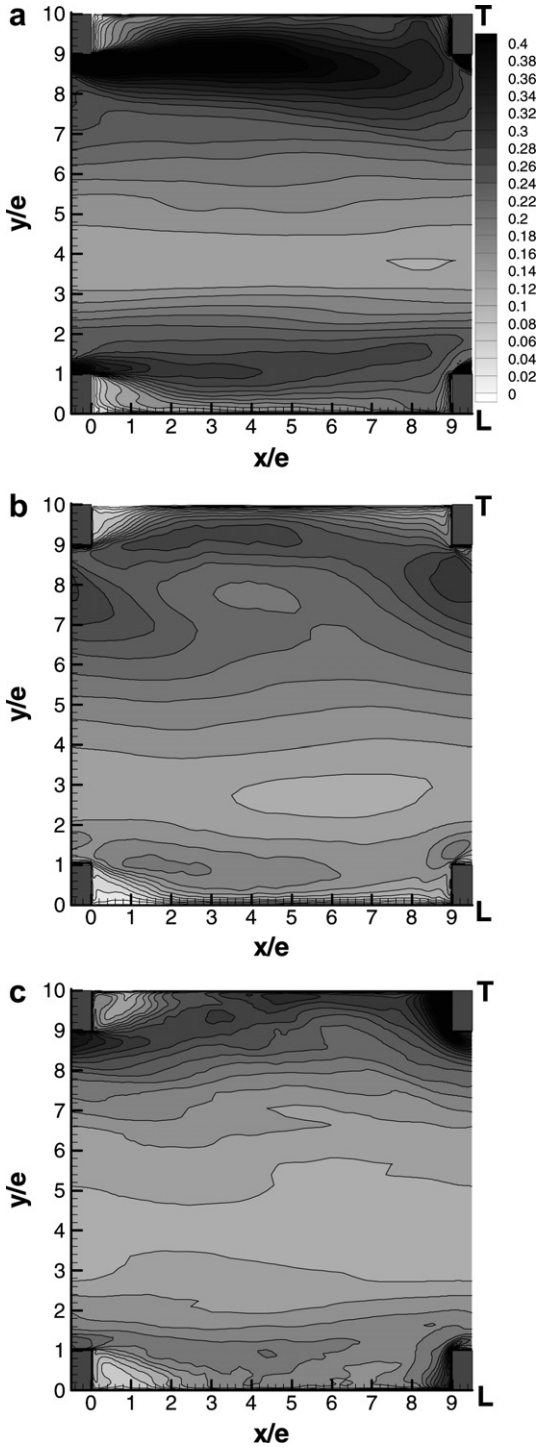

Fig. 9. Contours of the rms velocity fluctuations inside the ribbed channel for $Ro = 0.3$: (a) u_{rms}; (b) v_{rms}; (c) w_{rms}.

asymmetric as shown in Fig. 9. They are higher on the trailing side than those on the leading side. Although the rotation causes the quantitative difference between the trailing and leading sides, the structure of the velocity fluctuations looks qualitatively similar due to the presence of the rib. Note that w_{rms} has a local maximum near the reattachment point even on the leading side, which is consistent with the result that the heat transfer is enhanced near the reattachment point also on the leading wall as can be seen in Fig. 6b.

Fig. 10 shows the contours of the time-averaged Reynolds shear stress and heat flux inside the ribbed channel for $Ro = 0.3$. Like the velocity fluctuations, the rotation augments the Reynolds shear stress and turbulent heat flux on the trailing side and damps them on the leading side. The contours of the Reynolds shear stress lie parallel even near the wall except just behind the rib, whereas those having high turbulent heat flux form closed loops near the reattachment point (see the contours at $x/e = 3$–6). As described, the spatial distributions of the Reynolds shear stress and heat flux are different from each other, indicating the dissimilarity between the velocity and temperature in the ribbed channel (see below for more details).

3.2. Instantaneous velocity and temperature

Murata and Mochizuki [8] pointed out that the rotation breaks the similarity between the temperature and streamwise velocity. The Coriolis force appears only in the momentum equation, whereas the counter part does not exist in the energy equation (Eqs. (2) and (3)). In order to investigate the dissimilarity, first, we compare the

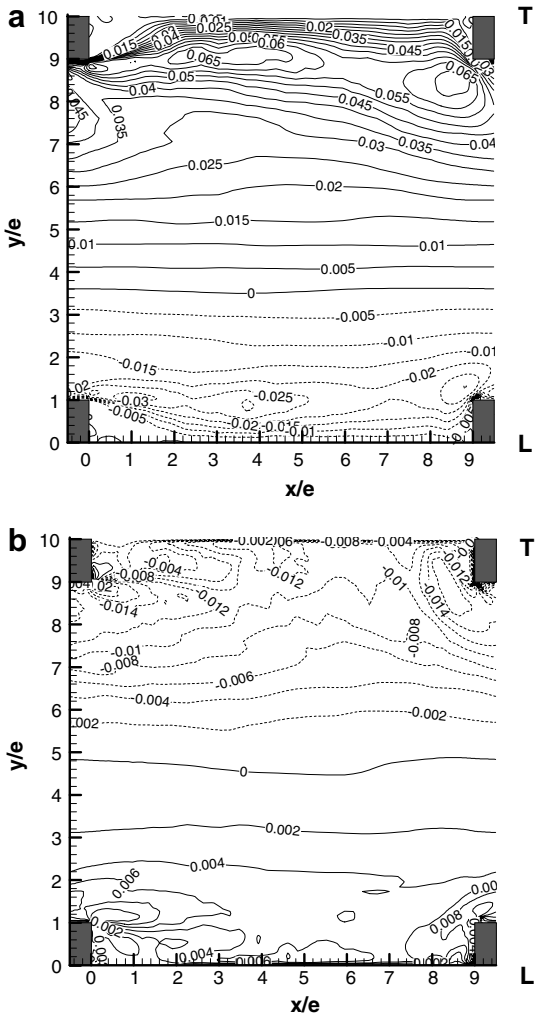

Fig. 10. Contours of the time-averaged Reynolds shear stress and heat flux ($Ro = 0.3$): (a) Reynolds shear stress $\overline{u'v'}$; (b) turbulent heat flux $\overline{\Theta'v'}$.

steamwise velocity and temperature fluctuations at $y^+ = 5$ for the smooth channel in Fig. 11. The similarity between the velocity and temperature in the case of $Ro = 0$ is quite sustained, but it is weakened on the leading side when $Ro = 0.3$. The scatter plots between $u'v'$ and $\Theta'v'$, which are not shown here, also show a similar behavior as those in Fig. 11. In contrast to that, as can be seen in Fig. 12, the similarity is severely destroyed in the ribbed channel due to the flow separation and reattachment even without the rotation, as expected.

By investigating the instantaneous flow and thermal fields, Ahn et al. [16] revealed the mechanism responsible for the existence of local peaks in the heat transfer distribution between ribs, i.e., the entrainment of cold fluid by vortical motions and the impingement of the entrained cold fluid on the front surface of rib. The same is true for the rotating ribbed channel, because the instantaneous flow and thermal fields in an $x - y$ plane look very similar, as shown in Fig. 13, to those for the non-rotating case reported by Ahn et al. [16]. Here, the vortices are identified

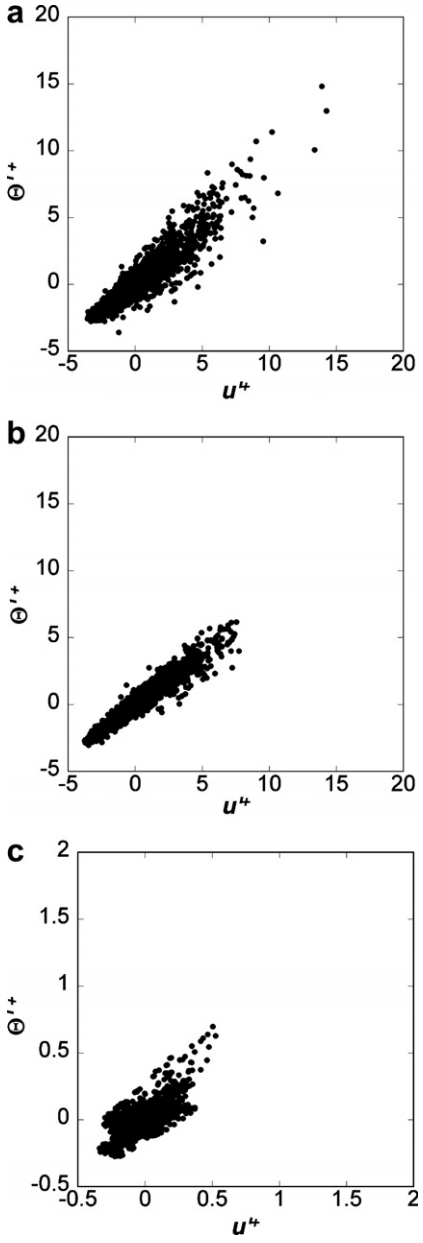

Fig. 11. Scatter plots between the streamwise velocity and temperature fluctuations at $y^+ = 5$ for the smooth channel: (a) $Ro = 0$; (b) $Ro = 0.3$, trailing wall; (c) $Ro = 0.3$, leading wall.

by the positive second invariant ($=Q$) of the velocity gradient tensor defined as [28]

$$Q = \frac{1}{2}\left(\frac{\partial u_i}{\partial x_j}\frac{\partial u_i}{\partial x_j} - \frac{\partial u_j}{\partial x_i}\frac{\partial u_j}{\partial x_i}\right). \tag{6}$$

In Fig. 13a, more vortices are found near the trailing wall due to the Coriolis force than near the leading wall. By these vortices, the cold fluid from the channel core region is more actively entrained to the trailing wall, which can be clearly observed from the instantaneous temperature contours near the trailing wall (see Fig. 13b).

In the ribbed channel, vortices are shed from the rib and play an important role in the transport of momentum and

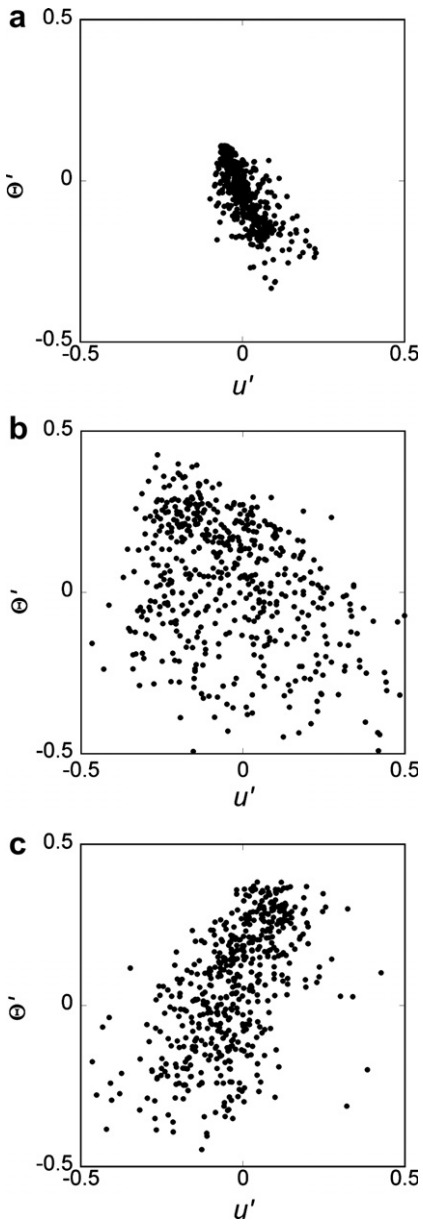

Fig. 12. Scatter plots between the streamwise velocity and temperature fluctuations inside the non-rotating ribbed channel at $y/e = 0.06$ from wall: (a) $x/e = 0.2$; (b) $x/e = 4.5$; (c) $x/e = 8.8$.

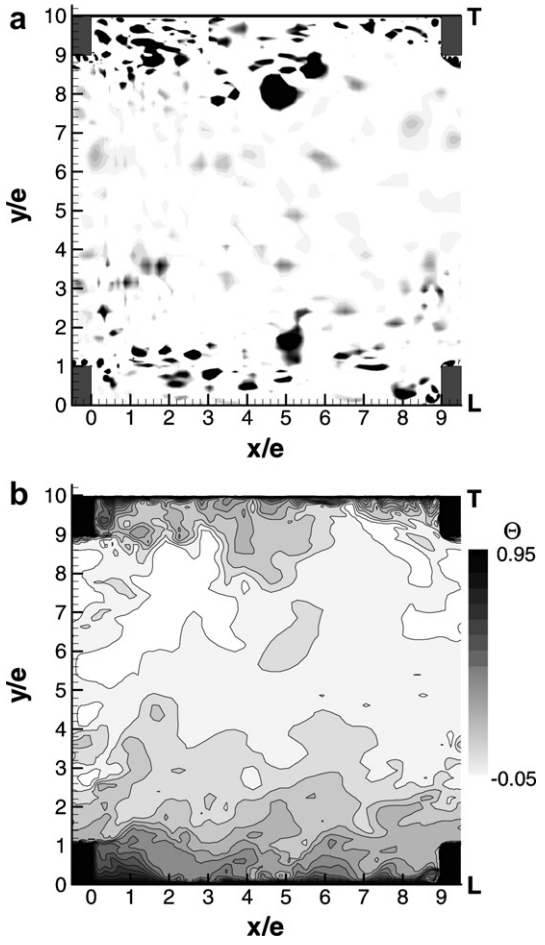

Fig. 13. Instantaneous flow and thermal structures inside the ribbed channel in an xy plane for $Ro = 0.3$: (a) vortical structures; (b) temperature contours.

heat, but these vortices do not exist in the smooth channel. The vortices shed from the rib are thus the key element explaining the difference in the rotation effect between the smooth and ribbed channels. Near the leading wall, these vortices prevent the turbulence from being suppressed by the rotation, and hence the variation of the temperature profile is less in the ribbed channel than in the smooth channel (see Figs. 3 and 4).

On the other hand, the temperature profile from the channel center to the trailing wall at $Ro = 0.1$ is changed slightly in the smooth channel, but significantly in the ribbed channel (see Figs. 3 and 4). The Coriolis force is balanced with wall-normal pressure gradient in a rotating channel, and a wall-normal motion is supposed to be amplified by breaking the balance [1]. The vortices shed from the rib should generate strong wall-normal motions, which may trigger the rotation effect at a lower rotation number.

Instantaneous velocity vectors and temperature fields in a $y - z$ plane at $x/e = 4.5$ are presented in Fig. 14. At $Ro = 0.3$, the vortices above the rib become stronger on the trailing side. With these vortices, many cold spots (bright gray) are entrained to the trailing side, and interact with the core flow. The temperature at the channel center region is much more uniform than that of the non-rotating case (see also Fig. 4).

4. Conclusions

We conducted large eddy simulations of flow and heat transfer in rotating/non-rotating and smooth/ribbed channels with a dynamic subgrid-scale model. Some important observations are noticed and summarized below.

(1) Turbulence and heat transfer are augmented on the trailing-wall side and attenuated on the leading-wall side in the rotating ribbed channel compared to the

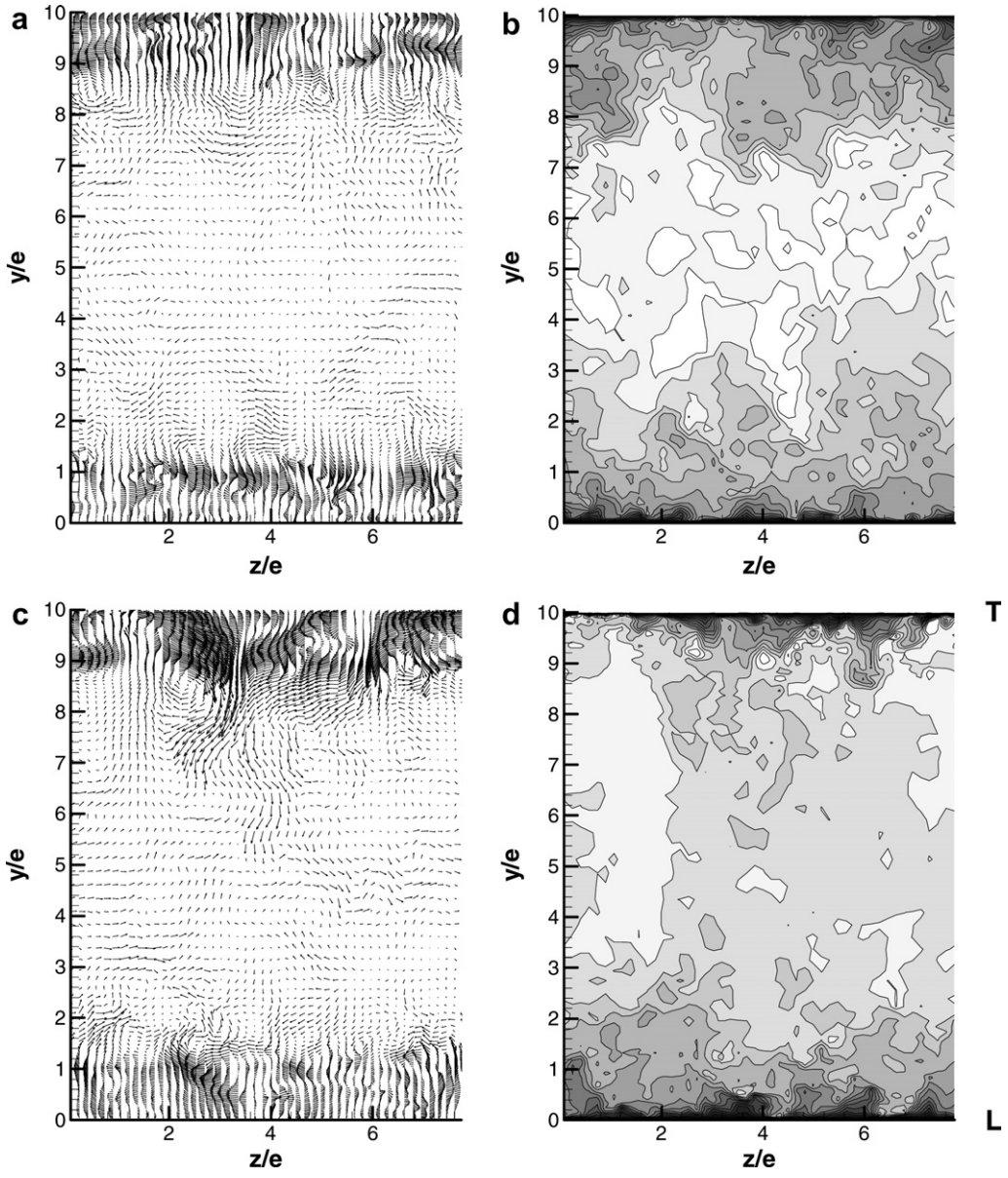

Fig. 14. Instantaneous velocity vectors (left) and temperature contours (right) in an yz plane at $x/e = 4.5$: (a) and (b) $Ro = 0$, (c) and (d) $Ro = 0.3$. Contours are from -0.05 to 0.95 by increments of 0.07.

stationary channel. The amount of increase in these quantities on the trailing-wall side is larger than the decrease on the leading-wall side.

(2) For the ribbed channel, the vortices shed from the rib induce the instability on the trailing-wall side, and thus the rotation effect is clearly observed even at the lower rotation number compared to the smooth channel.

(3) The rotation makes the separation bubble smaller on the trailing-wall side and bigger on the leading-wall side.

(4) The similarity between the streamwise velocity and temperature is broken due to both the rotation and the rib. The latter destroys the similarity more severely.

Acknowledgements

The authors gratefully acknowledge that this work is supported by the Micro Thermal System Research Center sponsored by the Korean Science and Engineering Foundation.

References

[1] B. Lakshminarayana, Fluid Dynamics and Heat Transfer of Turbomachinery, Wiley, 1996, pp. 315–322.

[2] J.C. Han, Heat transfer and friction in channels with two opposite rib roughened walls, ASME J. Heat Transfer 106 (1984) 774–781.

[3] T.-M. Liou, J.-J. Hwang, Turbulent heat transfer and friction in periodically fully developed channel flows, ASME J. Heat Transfer 114 (1992) 56–64.

[4] J.C. Han, J.S. Park, C.K. Lei, Heat transfer enhancement in channels with turbulence promoters, ASME J. Eng. Gas Turbine Power 107 (1985) 628–635.
[5] D.K. Tafti, S.P. Vanka, A numerical study of the effects of spanwise rotation on turbulent channel flow, Phys. Fluids A 3 (1991) 642–656.
[6] R. Kristoffersen, H. Andersson, Direct numerical simulations of low-Reynolds-number turbulent flow in a rotating channel, J. Fluid Mech. 256 (1993) 163–197.
[7] H. Wu, N. Kasagi, Turbulent heat transfer in a channel flow with arbitrary directional system rotation, Int. J. Heat Mass Transfer 47 (2004) 4579–4591.
[8] A. Murata, S. Mochizuki, Effect of cross-sectional aspect ratio on turbulent heat transfer in an orthogonally rotating rectangular smooth duct, Int. J. Heat Mass Transfer 42 (1999) 3803–3814.
[9] B.E. Launder, D.P. Tselepidakis, B.A. Younis, A second-moment closure study of rotating channel flow, J. Fluid Mech. 183 (1987) 63–75.
[10] S. Acharya, S. Dutta, T. Myrum, R.S. Baker, Periodically developed flow and heat transfer in a ribbed duct, Int. J. Heat Mass Transfer 36 (1993) 2069–2082.
[11] M. Ciafalo, M.W. Collins, Large eddy simulation of turbulent flow and heat transfer in plane and rib-roughened channels, Int. J. Numer. Meth. Fluids 15 (1992) 453–489.
[12] A. Murata, S. Mochizuki, Large eddy simulation with a dynamic subgrid-scale model of turbulent heat transfer in an orthogonally rotating rectangular duct with transverse rib turbulators, Int. J. Heat Mass Transfer 43 (2000) 1243–1259.
[13] Y. Miyake, K. Tsujimoto, M. Nakaji, Direct numerical simulation of rough-wall heat transfer in a turbulent channel flow, Int. J. Heat Fluid Flow 22 (2001) 237–244.
[14] Y. Nagano, H. Hattori, T. Houra, DNS of velocity and thermal fields in turbulent channel flow with transverse-rib roughness, Int. J. Heat Fluid Flow 25 (2004) 393–403.
[15] J. Cui, V.C. Patel, C.-L. Lin, Large-eddy simulation of turbulent flow in a channel with rib roughness, Int. J. Heat Fluid Flow 24 (2003) 372–388.
[16] J. Ahn, H. Choi, J.S. Lee, Large eddy simulation of flow and heat transfer in a channel roughened by square or semicircle ribs, ASME J. Turbomach. 127 (2005) 263–269.
[17] D.K. Tafti, Evaluating the role of subgrid stress modeling in a ribbed duct for the internal cooling of turbine blades, Int. J. Heat Fluid Flow 26 (2005) 92–104.
[18] J. Kim, D. Kim, H. Choi, An immersed-boundary finite-volume method for simulations of flow in complex geometries, J. Comput. Phys. 171 (2001) 132–150.
[19] J. Kim, H. Choi, An immersed-boundary finite-volume method for simulations of heat transfer in complex geometries, KSME Int. J. 18 (2004) 1026–1035.
[20] M. Germano, U. Piomelli, P. Moin, W.H. Cabot, A dynamic subgrid-scale closure model, Phys. Fluids A 3 (1991) 1760–1765.
[21] D.K. Lilly, A proposed modification of the Germano subgrid-scale closure model, Phys. Fluids A 4 (1992) 633–635.
[22] W. Cabot, P. Moin, Large eddy simulation of scalar transport with the dynamic subgrid-scale model, in: Large Eddy Simulation of Complex Engineering and Geophysical Flows, Cambridge University Press, 1993, pp. 141–158.
[23] J.A. Parsons, J.-C. Han, Y. Zhang, Effect of model orientation and wall heating condition on local heat transfer in a rotating two-pass square channel with rib turbulators, Int. J. Heat Mass Transfer 38 (1995) 1151–1159.
[24] A.G. Kravchenko, P. Moin, On the effect of numerical errors in large eddy simulations of turbulent flows, J. Comput. Phys. 131 (1997) 310–322.
[25] H.H. Cho, S.J. Wu, H.J. Kwon, Local heat/mass transfer measurements in a rectangular duct with discrete ribs, ASME J. Turbomach. 122 (2000) 579–586.
[26] T.-M. Liou, J.-J. Hwang, Effect of ridge shapes on turbulent heat transfer and friction in a rectangular channel, Int. J. Heat Mass Transfer 36 (1993) 931–940.
[27] Y.Y. Kim, K.M. Kim, D.H. Rhee, H.H. Cho, Effects of rotation speed on heat transfer in a 90° rib roughened two-pass duct, in: Proceedings of Internatonal Gas Turbine Congress, Paper No. TS-081, 2003.
[28] M. Tanaka, S. Kida, Characterization of vortex tubes and sheets, Phys. Fluids A 5 (1993) 2079–2082.